

Supporting Information

Resolving the Activity and Selectivity Trends for NH₃-SCR on Metal

Oxides by Microkinetic Simulation

Ying Liu,^{‡a} Yinkai Wu,^{‡a} Haifeng Wang,^{*a} Haiyang Yuan^{*a, b}

^a State Key Laboratory of Green Chemical Engineering and Industrial Catalysis, Center for Computational Chemistry and Research Institute of Industrial Catalysis, School of Chemistry and Molecular Engineering, East China University of Science and Technology, Shanghai, 200237, China

^b Key Laboratory for Ultrafine Materials of Ministry of Education, Shanghai Engineering Research Center of Hierarchical Nanomaterials, School of Materials Science and Engineering, East China University of Science and Technology, Shanghai 200237, China.

[‡] These authors contributed equally to this work.

Note S1. Calculation Method

Periodic DFT calculations were carried out in the VASP code¹, using the Perdew-Burke-Ernzerhof (PBE) functional with the generalized gradient approximation (GGA)². The project-augmented wave (PAW) method was used to represent the core-valence electron interaction.³ On the plane wave basis, an energy cutoff of 450 eV was employed. The Broyden method was employed for geometric relaxation until the maximal forces on each relaxed atom were less than 0.05 eV/Å. Here, a series of rutile-type transition metal oxides (MnO₂, RhO₂, RuO₂, MoO₂ and NbO₂) were selected, the (110) surface of which were modeled with four layers with a vacuum layer of 15 Å. During optimization, the bottom two layers of the slab were fixed and the top two layers and adsorbates were fully relaxed. A $p(3\times 1)$ surface slab with a corresponding $2\times 3\times 1$ k-point mesh was used. A constrained optimization scheme was used to search the transition state (TS).⁴ In order to correct for the on-site Coulomb effect of some transition metal oxides in GGA functional, the GGA+U approach was used here. The effective U value was set to 1.6 eV for the Mn-3d orbital of MnO₂.^{5, 6} In addition, the experimental studies showed that the ground state for MnO₂ is antiferromagnetic, thus an antiferromagnetic helical spin arrangement was imposed in all our calculations.⁷⁻⁹

The adsorption energies of adsorbates X on active sites were calculated with an equation: $E_{\text{ads}}(\text{X}) = E_{\text{x/surf}} - E_{\text{surf}} - E_{\text{x}}$, where E_{x} , E_{surf} and $E_{\text{x/surf}}$ represent the total energies of adsorbate X in the gas phase, clean surface and the surface with adsorbate X, respectively. The more negative $E_{\text{ads}}(\text{X})$ means the stronger adsorption of the adsorbates X on the active sites. Notably, in the NH₃-SCR system, the adsorption energy of the key intermediate NH₂ ($E_{\text{ads}}(\text{NH}_2@\text{M})$) and formation energy of O_{lat} vacancy ($E_f(\text{O}_{\text{vac}})$) are tested as activity descriptors, corresponding to describe the reactivity of metal site and O_{lat} on the metal oxides, respectively. The formation energy of oxygen vacancy ($E_f(\text{O}_{\text{vac}})$) was calculated by the equation $E_f(\text{O}_{\text{vac}}) = 0.5 * E_{\text{O}_2} + E_{\text{surf-vac}} - E_{\text{surf}}$, where E_{surf} , $E_{\text{surf-vac}}$ and E_{O_2} are the total energies of clean surface, the surface with O_{vac} and O₂ in the gaseous phase, respectively. Following this definition, the larger $E_f(\text{O}_{\text{vac}})$ corresponds to the more difficult formation of O_{vac}, or reflecting the stronger metal-O_{lat} bond to some extent. After calculating the adsorption energies of all adsorbates X on metal oxides ($E_{\text{ads}}(\text{X}@j)$, where X and j represent the adsorbates X and active sites, respectively), as well as the barrier (E_{a}) and enthalpy change (ΔH) of each elementary step in NH₃-SCR, NH₃ oxidation and NO oxidation as shown in Scheme S1, we correlated them with $E_{\text{ads}}(\text{NH}_2@\text{M})$ or $E_f(\text{O}_{\text{vac}})$ to examine their correlations and found a series of linear relationships. These linear relationships are discussed in detail in the manuscript, which shows the basic chemical trends of metal oxides.

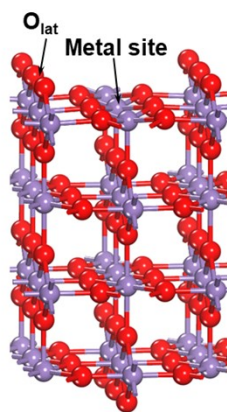
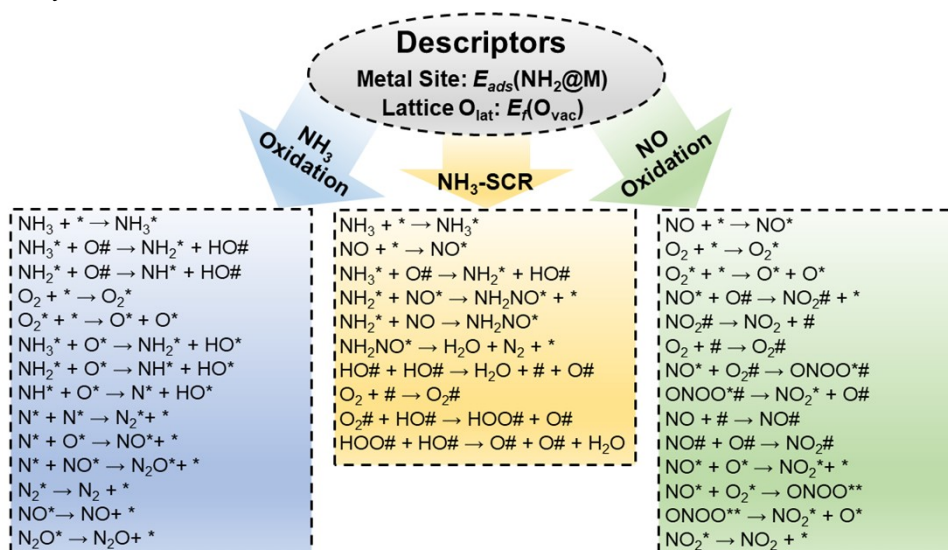


Fig. S1 Structure of rutile-type metal oxide (110) surface.

Scheme S1. Mechanisms of NH₃-SCR (orange), NH₃ oxidation (blue) and NO oxidation (green) on metal oxides. * and # represent metal site and O_{vac}, respectively, and O# is the lattice O_{lat}. $E_{ads}(NH_2@M)$ and $E_f(O_{vac})$ are selected as descriptors to describe the metal site and O_{lat}, respectively.



Note S2. Discussion for H removal process assisted by O₂(S)#

Originally, we considered the reaction O₂(S)# + HO# → HOO# + O#, where O₂(S)# is the most stable μ₂-bridged O₂ adsorption mode on O_{vac}. However, as shown in Fig. S2a, this reaction exhibits a weak correlation between the H-transfer barrier (E_a) and O_{vac} formation energy ($E_f(O_{vac})$). To probe the origin of this weak scaling, we analyzed the adsorption trends and found that $E_{ads}(O_2@O_{vac})$ and $E_{ads}(H@O_{lat})$ exhibit opposing dependencies on $E_f(O_{vac})$: stronger O₂ adsorption is accompanied by weaker O_{lat}-H binding (Fig. S2b). This implies that when O₂ binds too strongly to O_{vac}, it becomes less reactive toward hydrogen abstraction—i.e., the rate-limiting step shifts from H transfer to the structural rearrangement of O₂(S)# itself.

To decouple these effects, we introduced an intermediate adsorption configuration, O₂(I)#, where one O atom occupies O_{vac} while the second points outward (Fig. S2c). This allows us to separate the full H-removal process into two steps: (i) the structural transformation O₂(S)# → O₂(I)#, and (ii) O₂(I)# capturing an H from O_{lat}H group, O₂(I)# + HO# → HOO# + O#.

For step (i), good linear relationships were observed: $E_a = 0.27 * E_f(O_{vac}) + 0.49$ and $\Delta H = 0.35 * E_f(O_{vac}) - 0.18$ (Fig. 2d). These trends indicate that the energy cost to activate O₂(S)# increases with its stronger binding, supporting the idea that structural rearrangement dominates the barrier in this regime. In step (ii), where O₂(I)# abstracts an H from O_{lat}-H, we also observed linear correlations: $E_a = -0.25 * E_f(O_{vac}) - 1.07$ and $\Delta H = -0.42 * E_f(O_{vac}) + 0.62$. This reveals that H abstraction becomes more favorable with higher $E_f(O_{vac})$, i.e., when O_{lat}-H binding is weaker. Thus, the linearly adsorbed O₂(I)# serves as a more suitable reactive configuration for establishing meaningful activity-descriptor relationships, as it avoids the distortions imposed by overly stable O₂(S)# species.

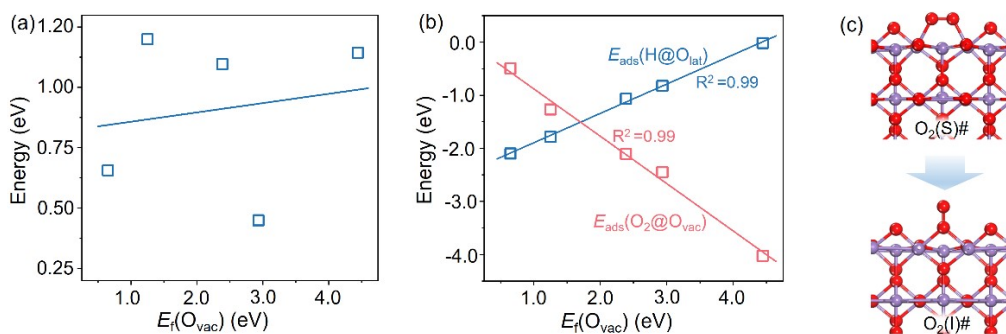


Fig. S2 (a) Scaling relations for the energy barrier (E_a) of the step $O_2(S)\# + HO\# \rightarrow HOO\# + O\#$ as a function of $E_f(O_{vac})$. (b) Scaling relations for the adsorption of O_2 on O_{vac} ($E_{ads}(O_2@O_{vac})$) as a function of $E_f(O_{vac})$. (c) Different O_2 adsorption configurations on O_{vac} .

Note S3. Linear Relationships for NH₃ oxidation

Based on the NH₃ oxidation mechanism (see blue part in Scheme S1),¹⁶⁻¹⁸ we extended this mechanism to rutile-type metal oxides (MnO₂, RhO₂, RuO₂, MoO₂ and NbO₂), and correlated the calculated energies (E_a and ΔH) with $E_{\text{ads}}(\text{NH}_2@M)$ or $E_{\text{f}}(\text{O}_{\text{vac}})$ to examine their dependencies. A series of linear relationships for NH₃ oxidation on rutile-type oxides were obtained.

First, for the process of NH₃ dissociation to N atom, two oxidative species (the lattice O_{lat} and the O species adsorbed on metal site) were considered to drive the reaction. As shown by Fig. S3a and Fig. S3b, it can be found that E_a and ΔH of the O_{lat}-assisted dehydrogenation of NH₃^{*}, NH₂^{*} and NH^{*} increase with the increase of $E_{\text{f}}(\text{O}_{\text{vac}}) - E_{\text{ads}}(\text{NH}_2@M)$. This indicates that NH₃ hydrogenation to form N atoms becomes more difficult when $E_{\text{f}}(\text{O}_{\text{vac}})$ is larger or $E_{\text{ads}}(\text{NH}_2@M)$ becomes more negative. Similarly, NH₃ dissociation into N atoms assisted by the O species adsorbed on metal site (O^{*}) also becomes more difficult with the increase of the metal-site binding strength (more negative $E_{\text{ads}}(\text{NH}_2@M)$), as evidenced by the decreasing trend of E_a and ΔH when $E_{\text{ads}}(\text{NH}_2@M)$ becomes positive (see Fig. S3c and S3d).

Second, for the subsequent N-N coupling step to form N₂, the negative slopes of the linear relationship, $E_a = -0.54 * E_{\text{ads}}(\text{NH}_2@M) - 0.84$ (Fig. S3e) and $\Delta H = -2.72 * E_{\text{ads}}(\text{NH}_2@M) - 11.01$ (Fig. S3f), show that this N-N coupling process becomes more difficult as the metal-site binding strength increases (more negative $E_{\text{ads}}(\text{NH}_2@M)$). Similarly, both E_a and ΔH of the N-O and N-NO coupling steps, forming NO and N₂O, respectively, also increase as $E_{\text{ads}}(\text{NH}_2@M)$ becomes more negative, indicating that these coupling processes are more challenging on metal sites with stronger binding strength.

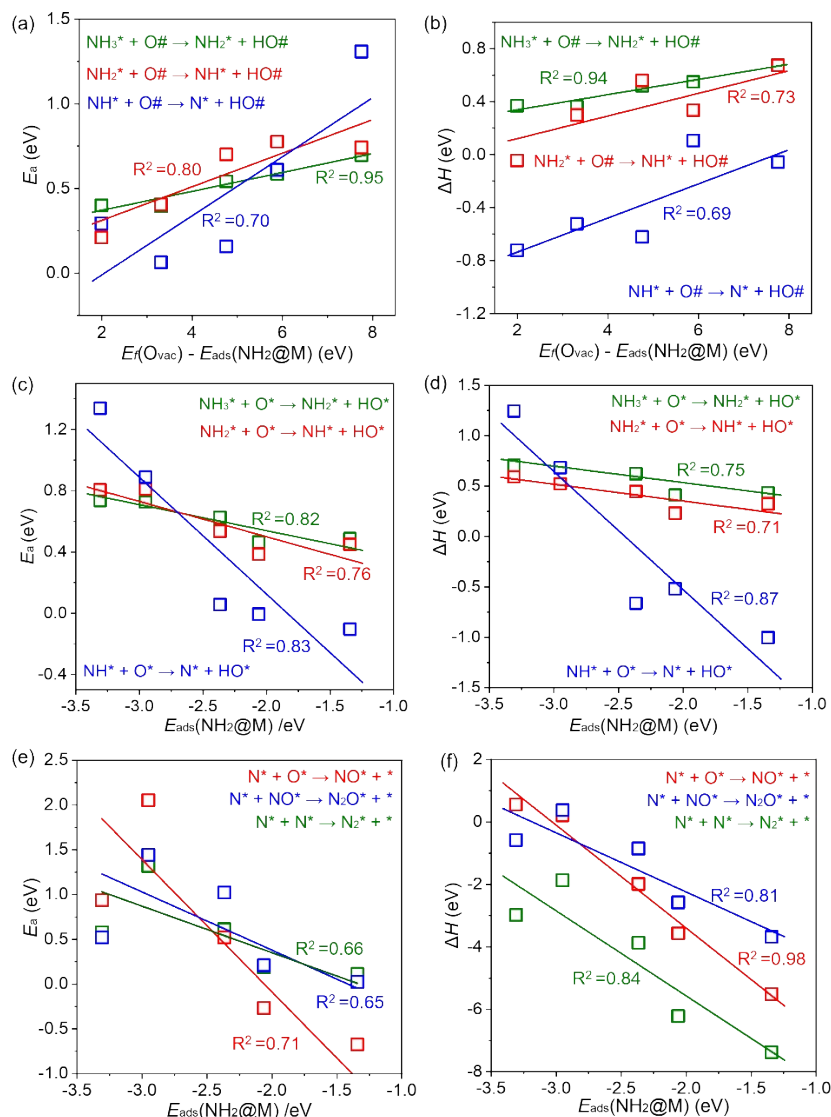


Fig. S3 Scaling relations for NH₃ oxidation as a function of $E_j(\text{O}_{\text{vac}}) - E_{\text{ads}}(\text{NH}_2@M)$ or $E_{\text{ads}}(\text{NH}_2@M)$. (a, b) The calculated barrier (E_a) and enthalpy change (ΔH) of the O_{lat} -assisted NH₃ dehydrogenation to form an N atom, $\text{NH}_3^* + \text{O}\# \rightarrow \text{NH}_2^* + \text{HO}\#$, $\text{NH}_2^* + \text{O}\# \rightarrow \text{NH}^* + \text{HO}\#$ and $\text{NH}^* + \text{O}\# \rightarrow \text{N}^* + \text{HO}\#$. (c, d) The calculated E_a and ΔH of the NH₃ dehydrogenation to form an N atom assisted by the O species adsorbed on metal site, $\text{NH}_3^* + \text{O}^* \rightarrow \text{NH}_2^* + \text{O}^*$, $\text{NH}_2^* + \text{O}^* \rightarrow \text{NH}^* + \text{O}^*$ and $\text{NH}^* + \text{O}^* \rightarrow \text{N}^* + \text{O}^*$. (e, f) The calculated E_a and ΔH of $\text{N}^* + \text{N}^* \rightarrow \text{N}_2^* + ^*$, $\text{N}^* + \text{O}^* \rightarrow \text{NO}^* + ^*$ and $\text{N}^* + \text{NO}^* \rightarrow \text{N}_2\text{O}^* + ^*$. The points from left to right are MnO₂, RhO₂, RuO₂, MoO₂ and NbO₂, respectively. * and # represent the metal and O_{vac} sites on metal oxides, respectively, O# is the lattice O_{lat} .

Note S4. Kinetic details

According to the De Donder relation¹⁰, the net rate for elementary step i in terms of the forward rate constant, k_i , the coverage of the reactant on two different sites (* represents Mn_{5c} site and represents O_{vac} site), $\theta(j)$, and the reversibility, Z_i , can be written as

$$r_i = k_i \prod_j \theta(j)^{v_{ij}} (1 - Z_i) \quad (\text{Eqn-S1})$$

where $Z_i = \prod_j \theta(j)^{v_{ij}} / K_{eq,i}$, which approaches zero as step i becomes irreversible and approach unity as step becomes in quasi-equilibrium. $K_{eq,i}$ is the equilibrium constant of step i , determined by the standard Gibbs free energy change of the reaction, $K_{eq,i} = \exp(-\Delta G_i / RT)$. v_{ij} are the stoichiometric coefficients for the j reactants or products of step i . Z_i can be solved by following the steady state condition. In our microkinetic model, we can solve the kinetic equations together with the condition that the total coverage of all species on metal site or the lattice O_{lat} is equal to 1 ML, respectively. Then, the overall rate of the reaction can be calculated.

Notably, the collision theory¹¹ was used to estimate the barriers (E_a) of gas-phase molecule adsorption process, as well as the barrier of the gas-phase NO coupling with the surface NH_2^* species. Therefore, according to the transition state theory and collision theory, the reaction rate on a per-site basis can be written as:

$$r_i(T) = \frac{k_B T}{h} \exp\left(-\frac{E_a}{k_B T}\right) \frac{P_i}{P^0} \approx S_i(T) \frac{P_i A}{\sqrt{2\pi k_B m_i T}} \quad (\text{Eqn-S2})$$

where k_B , h , T , P_i and m_i are Boltzmann constant, Planck constant, reaction temperature, pressure, and mass of gas molecule, respectively. Additionally, A is the area of the atom described as $A = \pi r^2$, in which r is the van der Waals (VDW) radius of the atom. Here, we assumed that the gas behaves ideally, and the sticking coefficient $S_i(T)$ is approximated as 1. Thus, we can derive an equation for E_a :

$$E_a \approx -k_B T \ln\left(\frac{P^0 A h}{k_B T \sqrt{2\pi k_B m_i T}}\right) \quad (\text{Eqn-S3})$$

In our microkinetic model, for the surface elementary steps without adsorption/desorption, the entropy effect is typically small and can be largely cancelled between the initial state and transition state or final state;^{12, 13} for the adsorption/desorption processes of gaseous molecule, the large entropy contribution of gaseous molecules ($T\Delta S$) was considered to calculate Gibbs free energy change (ΔG) at a given temperature, which was obtained from the experimental values.¹⁴ Here, we used the experimental condition¹⁵: $P_{\text{NH}_3} = 5.00 \times 10^{-4}$ atm, $P_{\text{NO}} = 5.00 \times 10^{-4}$ atm, $P_{\text{O}_2} = 0.02$ atm, $P_{\text{N}_2} = 0.8$ atm and $P_{\text{H}_2\text{O}} = 0.05$ atm. We employed a fully first-principles microkinetic model under the mean-field approximation, implemented using the CATKINAS package. This framework includes robust solvers such as the sensitivity-supervised interlock algorithm, particle swarm optimization, and modified Newton's method¹⁹⁻²¹, enabling efficient treatment of complex reaction networks.

Our kinetic model integrates a comprehensive reaction network encompassing the main NH_3 -SCR pathway (via NH_2NO formation), as well as competitive NH_3 and NO oxidation side reactions (Scheme S1). We explicitly incorporate the possible Langmuir-Hinshelwood, Eley-Rideal, and Mars-van Krevelen mechanisms. This mechanistic breadth enables our model to capture selectivity trends and side-product formation with higher fidelity than models limited to narrower pathways. In addition, our microkinetic model is constructed entirely from DFT-derived thermodynamic and kinetic parameters. This enables enhanced transferability across catalyst systems and operating conditions. The utility of microkinetic model for catalytic reaction has been supported, and our

model demonstrates strong consistency with experimental observations in NH₃-SCR on some catalysts, e.g., Fe₂O₃ and CeO₂.^{22, 23} These support the robustness of our model for capturing NH₃-SCR kinetics across different catalyst systems.

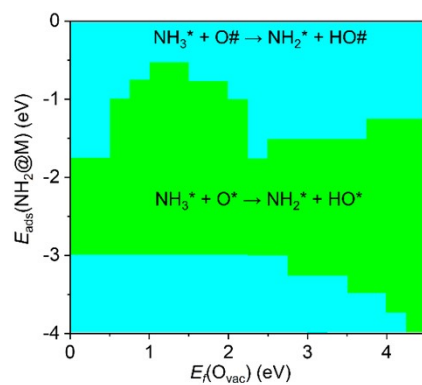


Fig. S4 Selectivity map of the NH_3 dehydrogenation to NH_2 assisted by O_{lat} ($\text{O}\#$) and the O species adsorbed on metal site (O^*), respectively. * and # represent the metal site and the lattice oxygen vacancy (O_{vac}), and $\text{O}\#$ is the lattice O_{lat} .

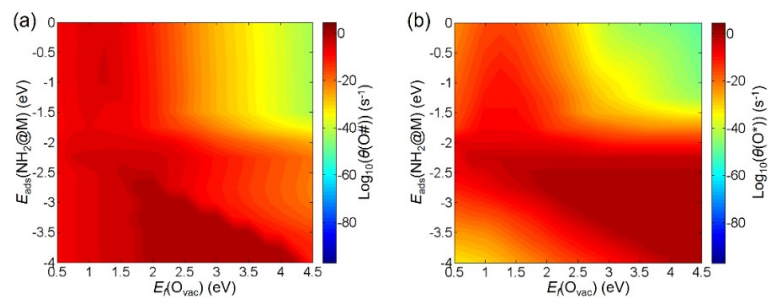


Fig. S5 Coverage change trends of (a) the lattice O_{lat} ($\theta(O\#)$), and (b) the O species adsorbed on metal site ($\theta(O^*)$) as a function of $E_f(O_{vac})$ and $E_{ads}(NH_2@M)$.

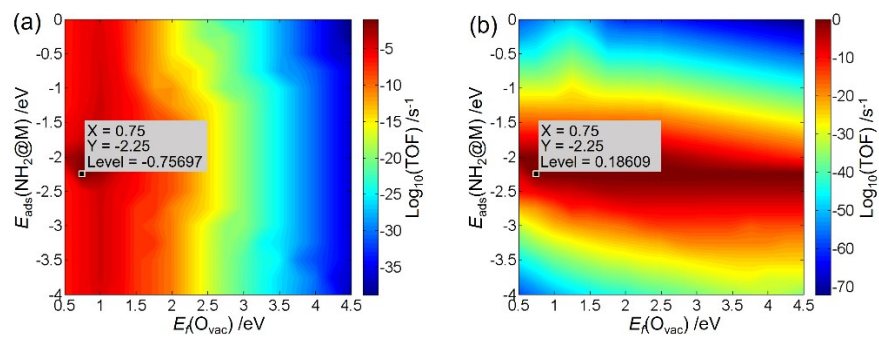


Fig. S6 Rate trends of NO oxidation on rutile-type metal oxides via (a) Mars-van-Krevelen mechanism and (b) Langmuir-Hinshelwood mechanism as a function of $E_f(O_{vac})$ and $E_{ads}(NH_2@M)$.

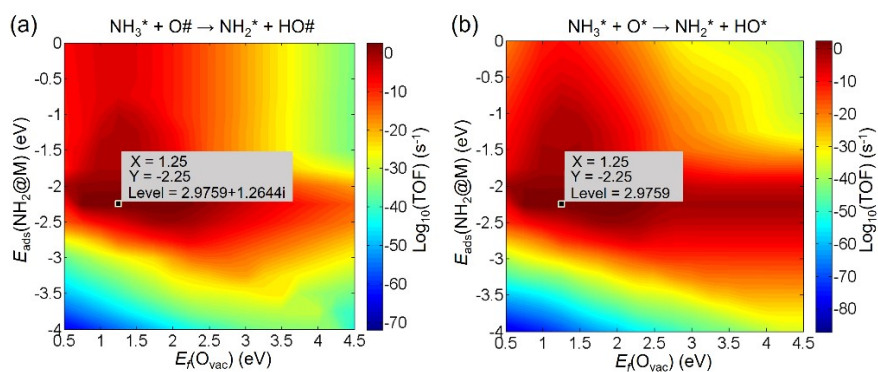


Fig. S7 Rate trends of NH_3 dehydrogenation assisted by (a) O_{lat} , $\text{NH}_3^* + \text{O}\# \rightarrow \text{NH}_2^* + \text{HO}\#$ and (b) adsorbed O on metal site, $\text{NH}_3^* + \text{O}^* \rightarrow \text{NH}_2^* + \text{HO}^*$, on rutile-type metal oxides as a function of $E_f(\text{O}_{\text{vac}})$ and $E_{\text{ads}}(\text{NH}_2\text{@M})$, respectively.

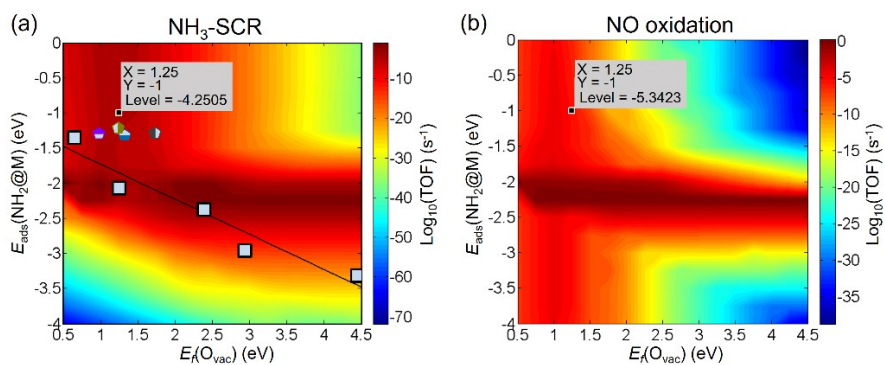


Fig. S8 3D volcano-shaped activity maps of (a) NH_3 -SCR and (b) NO oxidation as a function of $E_f(\text{O}_{\text{vac}})$ and $E_{\text{ads}}(\text{NH}_2@M)$, where the black line is the linear relationship between $E_{\text{ads}}(\text{NH}_2@M)$ and $E_f(\text{O}_{\text{vac}})$. The black points from left to right in Fig. S8a are MnO_2 , RhO_2 , RuO_2 , MoO_2 and NbO_2 , respectively. The colored points from left to right in Fig. S8a are Rh- MnO_2 , Nb- MnO_2 , Ru- MnO_2 and Mo- MnO_2 , respectively.

Table S1. Adsorption energies of NH_2 ($E_{\text{ads}}(\text{NH}_2@M)$) and formation energies of O_{vac} ($E_f(\text{O}_{\text{vac}})$) on metal(Rh, Ru, Mo, Nb)-doped $\text{MnO}_2(110)$.

	Rh-doped MnO_2	Ru-doped MnO_2	Mo-doped MnO_2	Nb-doped MnO_2
$E_{\text{ads}}(\text{NH}_2@M)$	-1.29 eV	-1.31 eV	-1.28 eV	-1.26 eV
$E_f(\text{O}_{\text{vac}})$	0.97 eV	1.32 eV	1.73 eV	1.24 eV

References

- (1) G. Kresse, J. Furthmüller, *Phys. Rev. B.*, 1996, **54**, 1169-1186.
- (2) J. P. Perdew, A. Ruzsinszky, G. I. Csonka, O. A. Vydrov, G. E. Scuseria, L. A. Constantin, X. Zhou, K. Burke, *Phys. Rev. Lett.*, 2008, **100**, 136406.
- (3) G. Kresse, D. Joubert, *Phys. Rev. B.*, 1999, **59**, 1758-1775.
- (4) A. Alavi, P. Hu, T. Deutsch, P. L. Silvestrelli, J. Hutter, *Phys. Rev. Lett.*, 1998, **80**, 3650.
- (5) H. Y. Yuan, N. N. Sun, J. F. Chen, J. M. Jin, H. F. Wang, P. Hu, *ACS Catal.*, 2018, **8**, 9269-9279.
- (6) G. A. Oxford, A. M. Chaka, *J. Phys. Chem. C*, 2011, **115**, 16992-17008.
- (7) Y. Paik, J. P. Osegovic, F. Wang, W. Bowden, C. P. Grey, *J. Am. Chem. Soc.*, 2001, **123**, 9367-9377.
- (8) C. Franchini, R. Podloucky, J. Paier, M. Marsman, G. Kresse, *Phys. Rev. B.*, 2007, **75**, 195128.
- (9) T. A. Mellan, K. P. Maenetja, P. E. Ngoepe, S. M. Woodley, C. R. A. Catlow, R. Grau-Crespo, *J. Mater. Chem. A.*, 2013, **1**, 14879-14887.
- (10) J. A. Dumesic, *J. Catal.*, 1999, **185**, 496-505.
- (11) Q. L. Tang, Q. J. Hong, Z. P. Liu, *J. Catal.*, 2009, **263**, 114-122.
- (12) J. K. Nørskov, T. Bligaard, A. Logadottir, J. R. Kitchin, J. G. Chen, S. Pandalov, U. Stimming, *J. Electrochem. Soc.*, 2005, **152**, J23-J26.
- (13) D. Wang, J. Jiang, H. F. Wang, P. Hu, *ACS Catal.*, 2016, **6**, 733-741.
- (14) M. W. Chase, *J. Phys. Chem. Ref. Data, Monograph 9*, 1998, 1-1951.
- (15) F. Kapteijn, L. Singoredjo, A. Andreini, J. A. Moulijn, *Appl. Catal. B-Environ.*, 1994, **3**, 173-189.
- (16) Y. Wang, K. Jacobi, W. D. Schöne, G. Ertl, *J. Phys. Chem. B*, 2005, **109**, 7883-7893.
- (17) N. Lopez, M. Garcia-Mota, J. Gomez-Diaz, *J. Phys. Chem. C*, 2008, **112**, 247-252.
- (18) S. I. Shah, S. Hong, T. S. *J. Phys. Chem. C*, 2014. **118**, 5226-5238.
- (19) J. Chen, M. L. Jia, P. Hu, H. F. Wang, *J. Comput. Chem.* 2021, **42**, 379-391.
- (20) J.F. Chen, M.L. Jia, Z.Z. Lai, P. Hu, H. F. Wang, *J. Chem. Phys.* 2021, **154**, 024108.
- (21) J.F. Chen, Y. Mao, H.F. Wang, P. Hu, *ACS Catal.* 2016, **6**, 7078-7087.
- (22) H. Y. Yuan, N. Sun, J. Chen, H. G. Yang, P. Hu, H. Wang, *JACS Au* 2022, **2**, 2352-358.
- (23) D. Xiong, Y. Chen, H. Yuan, H. Wang, *Phys. Chem. Chem. Phys.* 2024, **26**, 25452.